ELSEVIER

J. Non-Newtonian Fluid Mech. 143 (2007) 38–47

Journal of Non-Newtonian Fluid Mechanics

www.elsevier.com/locate/jnnfm

Flow development in compression of a finite amount of a Bingham plastic

Georgios C. Florides [a], Andreas N. Alexandrou [a], Georgios C. Georgiou [b,*]

[a] *Mechanical and Manufacturing Engineering, University of Cyprus, Cyprus*

[b] *Department of Mathematics and Statistics, University of Cyprus, P.O. Box 20537, 1678 Nicosia, Cyprus*

Received 6 June 2006; received in revised form 12 November 2006; accepted 11 January 2007

Abstract

The flow and shape evolution during the compression of a finite amount of a Bingham plastic is investigated by means of numerical simulations. The problem relates to the popular compression test used for the rheological characterization of non-Newtonian fluids. The flow is modelled in Lagrangian coordinates using the Papanastasiou regularization for the Bingham plastic and a mixed-Galerkin finite element method. Simulations have been performed for compression under both constant load and constant velocity. Results for various Reynolds and Bingham numbers are presented and discussed.

Keywords: Bingham plastics; Squeeze flow; Compression test; Computational rheology; Finite elements

1. Introduction

The motivation of the present work derives from our interest in semisolid metal slurries. These are mixtures of rounded, rosette-like solid particles and liquid at temperatures between the liquidus and solidus limits. The average solid volume fraction is a function of the bulk temperature of the suspension and varies from zero to unity. During processing the viscosity also changes significantly due to the evolution of the internal structure [1]. In general, semisolid materials behave as viscoplastic fluids characterized by a finite yield stress, τ_0, and other material properties that vary with time and the shear rate [1]. Therefore, semisolid slurries can be modelled as Bingham plastic or Herschel–Bulkley fluids with time-dependent material parameters the determination of which is obviously quite important.

Let $\mathbf{u}$ and $\underline{\underline{\tau}}$ be respectively the velocity vector and the viscous stress tensor, and $\underline{\underline{\dot{\gamma}}}$ be the rate of strain tensor:

$$\underline{\underline{\dot{\gamma}}} = \nabla\mathbf{u} + (\nabla\mathbf{u})^{\mathrm{T}} \tag{1}$$

where $\nabla\mathbf{u}$ is the velocity-gradient tensor and the superscript T denotes its transpose. The magnitudes of $\underline{\underline{\dot{\gamma}}}$ and $\underline{\underline{\tau}}$, denoted respectively by $\dot{\gamma}$ and τ, are defined by

$$\dot{\gamma} = \sqrt{\frac{1}{2}\mathrm{II}_{\dot{\gamma}}} = \sqrt{\frac{1}{2}\underline{\underline{\dot{\gamma}}} : \underline{\underline{\dot{\gamma}}}} \quad \text{and} \quad \tau = \sqrt{\frac{1}{2}\mathrm{II}_{\tau}} = \sqrt{\frac{1}{2}\underline{\underline{\tau}} : \underline{\underline{\tau}}} \tag{2}$$

where II stands for the second invariant of a tensor. Then, the Bingham model is written as follows:

$$\underline{\underline{\dot{\gamma}}} = \underline{\underline{0}}, \quad \tau \le \tau_0; \qquad \underline{\underline{\tau}} = \left(\frac{\tau_0}{\dot{\gamma}} + \mu\right)\underline{\underline{\dot{\gamma}}}, \quad \tau \ge \tau_0 \tag{3}$$

where μ is the constant viscosity. The two material parameters, μ and τ_0 are determined from experimental data.

The ideal Bingham plastic model is difficult to use in theoretical and numerical analyses, since it is discontinuous and singular when the shear rate approaches zero. It is thus primarily used in simple unidirectional problems. For the numerical simulation of complicated two-dimensional flows of Bingham fluids, regularized continuous versions of the constitutive equation (3) are used in order to avoid the need of determining the yielded ($\tau > \tau_0$) and unyielded ($\tau \le \tau_0$) regions in the flow. The most popular regularization is the one proposed by Papanastasiou [2,3]:

$$\underline{\underline{\tau}} = \left\{\frac{\tau_0[1 - \exp(-m\dot{\gamma})]}{\dot{\gamma}} + \mu\right\}\underline{\underline{\dot{\gamma}}} \tag{4}$$

where m is a stress growth exponent. Eq. (4) provides a satisfactory approximation of the Bingham plastic model for sufficiently large values of m and is valid uniformly at all levels of $\dot{\gamma}$ [2–6].

* Corresponding author. Tel.: +357 22892612; fax: +357 22892601.
E-mail address: georgios@ucy.ac.cy (G.C. Georgiou).

0377-0257/$ – see front matter © 2007 Elsevier B.V. All rights reserved.
doi:10.1016/j.jnnfm.2007.01.004

It should be noted, however, that the value of m should be chosen very carefully, since large values might lead to convergence difficulties while small values can lead to wrong results [3,4,6]. Alexandrou and his collaborators [4,7] demonstrated that regularized models such as the Papanastasiou, the biviscosity and other viscoplastic models, could predict the flow and a posteriori represent reasonably well the topography of the yield surfaces ($\tau = \tau_0$), provided that the regularization parameters are selected properly.

The squeeze flow of viscoplastic materials has received considerable attention in the past two decades and different constitutive equations have been used, in both theoretical and numerical studies, such as the bi-viscosity model in the early works of Gartling and Phan Thien [8] and O'Donovan and Tanner [9], the original Bingham model by Smyrnaios and Tsamopoulos [10] and Roussel et al. [11], the Herschel–Bulkley model by Sherwood and Durban [12], an elasto-viscoplastic model by Adams et al. [13], and the regularized Papanastasiou model by Smyrnaios and Tsamopoulos [10], Matsoukas and Mitsoulis [14], Mitsoulis and Matsoukas [15], and Karapetsas and Tsamopoulos [16]. In most of these works, both plates were assumed to move either at constant velocity or at constant load. However, in the numerical work of Adams et al. [13] and in the analysis of Sherwood and Durban [12] the lower plate was assumed to be fixed.

Another assumption usually made in both numerical and theoretical studies of squeeze flow is that of the quasi-steady flow [8–10,14]. Karapetsas and Tsamopoulos [16] solved the transient axisymmetric squeeze flow of a viscoplastic material under creeping flow conditions using the Papanastasiou model, for both cases where the disks are moving with constant velocity and under constant force. As pointed out by these authors, this distinction is impossible under the quasi-steady-state conditions.

In agreement with previous quasi-steady-state studies [9,10,13–15], Karapetsas and Tsamopoulos reported that in squeeze flow under constant velocity, unyielded material arises only around the two centers of the disks [16]. Adams et al. [13] who considered the case in which the lower plate is fixed, also reported the existence of such wedge regions. Moreover, they reported that unyielded regions appear also at the periphery of the specimen. Adams et al. considered an elasto-viscoplastic material assuming that linear elastic deformation occurs prior to yield and that the yield surface is strain rate hardening according to an associated viscoplastic flow rule [13]. They also considered both non-slip and lubricated wall boundary conditions. Mitsoulis and Matsoukas [15] also observed unyielded regions at the free surface, in some cases of quasi-steady-state planar squeeze flow and large aspect ratios. They noted, however, that this phenomenon may be due to the regularized Papanastasiou model used.

In squeeze flow under constant velocity, the size of the unyielded regions was found to increase with the Bingham number and to decrease as the two plates approach each other [10,14–16]. Matsoukas and Mitsoulis [14] noted that big aspect ratios give larger unyielded regions than small ones for the same Bingham number, and that axisymmetric geometries give smaller unyielded regions than planar ones. Karapetsas and Tsamopoulos [16] also observed that the size of the unyielded region decreases when slip occurs along the plates. They also showed that the load required for maintaining the velocity of the disks constant increases significantly with the Bingham number and the time, which provides a technique for calculating the yield stress [16].

For the case of squeeze flow under constant load, Karapetsas and Tsamopoulos [16] reported that the disks decelerate until they finally stop, when the material behaves as a rigid solid. The unyielded regions of the material arise first around the two stagnation points of the flow and then at the outer edge of the sample. As the time proceeds, the latter extend towards the axis and the plane of symmetry and eventually merge with the former unyielded regions to form a rigid domain. Note that bounds for the limiting film thickness (at which the velocity vanishes) are given by Zwick et al. [17] who carried out the variational analysis of the creeping squeeze flow of a Herschel–Bulkley fluid under constant load.

In some of the aforementioned works, the free surface of the sample was assumed to be flat [10,14] or was completely ignored by letting the material to freely exit the region defined by the two plates [8,9]. In their squasi-steady-state simulations, Mitsoulis and Matsoukas [15] noted that the inclusion of the free surface does not alter the unyielded regions in any visible way. More recently, Karapetsas and Tsamopoulos [16] employed a sophisticated quasi-elliptic mesh generation scheme in order to follow the large deformations of the free surface of the fluid, not only inside but also outside the space of the two disks.

In actual compression experiments under constant load, the material parameters are determined by means of compression velocity data, under simplifying assumptions for the compression. The magnitude of the rate of strain is typically estimated from the original dimension of the sample and the velocity of the press. An effective viscosity is then evaluated using measured bulk quantities that are not fixed beforehand. Unfortunately, this procedure ignores the fact that, irrespective of the sample's size, the resulting flow is not viscometric and the sample responds to the compression in the same complex manner as a larger sample. Other useful information that is also neglected is the evolution of the sample's shape during compression. Using computational rheology, as proposed here, one can first measure all pertinent quantities in the compression experiment, and then use accurate computational models to select, by trial-and-error or other more sophisticated matching methods, the flow model and material constants that reproduce the measured experimental data and match the history of deformation of the sample [4].

In this study, we investigate numerically the compression of a finite amount of Bingham-plastic fluid assuming that the material parameters are time-independent. The numerical simulations are performed either under constant load or under constant velocity applied only on the upper disk. As already mentioned, among the aforementioned literature, the lower disk is fixed only in the works of Sherwood and Durban [12] and Adams et al. [13]. Other important differences between the present and previous

studies are: (a) the creeping flow assumption is relaxed (i.e. the Reynolds number is not zero) and (b) the initial sample aspect ratio is 2, in agreement with experiments with semisolid materials, whereas in the literature this ratio is usually equal to or less than unity (if not negligibly small). The objective here is to study how the rate of compression and other derived quantities are affected by the controlling parameters such as the yield stress. A key derived-quantity examined here is the topology of the yielded and unyielded zones and their evolution during processing. This aspect is important in understanding the structural changes and rheological attributes during flow.

In Section 2, the governing equations and boundary and initial conditions are presented. In Section 3, the numerical method is briefly discussed. In Section 4, the numerical results are presented and discussed. Concluding remarks are provided in Section 5.

2. Governing equations

Fig. 1 shows the axisymmetric sample of initial radius R and height $H = 2R$ used in the simulations. The material is placed on a plate and compressed from the top by applying either constant load or constant velocity. Due to symmetry, only one-half of the sample is used in the simulations. A related flow is Stefan's squeezing flow, in which both sides are compressed.

The flow is governed by the continuity and momentum equations for an incompressible fluid:

$$\nabla \cdot \mathbf{u} = 0 \tag{5}$$

and

$$\rho \frac{\mathrm{D}\mathbf{u}}{\mathrm{D}t} = -\nabla p + \nabla \cdot \underline{\underline{\tau}} \tag{6}$$

where gravity is neglected, ρ is the density of the fluid, p is the pressure, and D**u**/Dt is the material derivative. The viscous stress tensor is assumed to obey the regularized Papanastasiou equation (4), which closes the system of Eqs. (5) and (6).

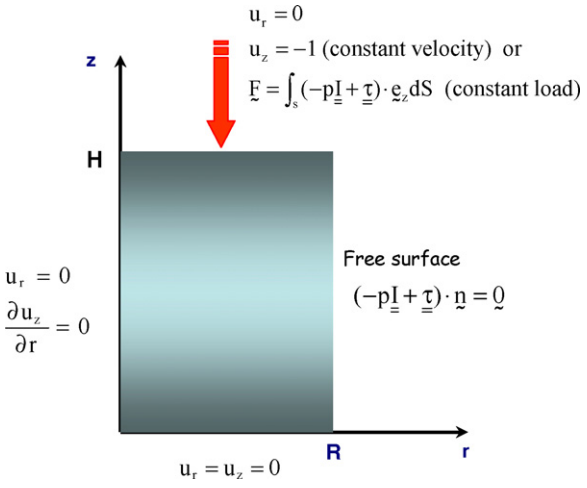

Fig. 1. Geometry and boundary conditions of the compression experiment. At $t = 0$ the sample is at rest.

The governing equations (4)–(6) are non-dimensionalized using the following scales:

$$x_i^* = \frac{x_i}{H}, \qquad \underline{\underline{\tau}}^* = \frac{\underline{\underline{\tau}}}{\tau_0}, \qquad p^* = \frac{p}{\tau_0}, \qquad \mathbf{u}^* = \frac{\mathbf{u}}{U},$$
$$t^* = \frac{t}{H/U} \tag{7}$$

where U is the compression velocity of the sample. In the case of compression under constant load, U is just an arbitrary velocity and the load, $\bar{F}$, is scaled by $\tau_0 H^2$, i.e. the dimensionless load is given by

$$F = \frac{\bar{F}}{\tau_0 H^2} \tag{8}$$

The stars here denote non-dimensionalized quantities. By means of the above scalings, the governing equations (5) and (6) become:

$$\nabla \cdot \mathbf{u}^* = 0 \tag{9}$$

and

$$Re \frac{\mathrm{D}\mathbf{u}^*}{\mathrm{D}t^*} = -\nabla p + \nabla \cdot \tau^* \tag{10}$$

where Re is the Reynolds number:

$$Re = \frac{\rho U H}{\mu} \tag{11}$$

The dimensionless form of the Papanastasiou regularized constitutive relation is

$$\underline{\underline{\tau}}^* = \left[Bn \frac{1 - \exp(-M\dot{\gamma}^*)}{\dot{\gamma}^*} + 1 \right] \underline{\underline{\dot{\gamma}}}^* \tag{12}$$

where $\underline{\underline{\dot{\gamma}}}^*$ is the dimensionless rate of strain tensor, $\dot{\gamma}^*$ denotes its second invariant, M is the dimensionless growth exponent, and Bn is the Bingham number. The last two-dimensionless numbers are defined as follows:

$$M = \frac{mU}{H} \quad \text{and} \quad Bn = \frac{\tau_0 H}{\mu U} \tag{13}$$

For simplicity, the stars are dropped hereafter.

The boundary conditions of the flow are shown in Fig. 1. Symmetry boundary conditions are imposed along the axis of symmetry and the velocity is set to zero along the bottom. On the free surface it is assumed that the surface tension is zero. When the specimen is compressed at constant velocity (from the top), the transverse velocity is set to −1. When the specimen is compressed at constant load in the direction of gravity, i.e. the dimensionless load, scaled by $\tau_0 H^2$, is of the form $\mathbf{F} = -F\mathbf{e}_z$, the boundary condition at the top of the sample is given by

$$\mathbf{F} = \int_s (-p\underline{\underline{I}} + \underline{\underline{\tau}}) \cdot \mathbf{e}_z \, \mathrm{d}S \tag{14}$$

where S is the surface of the top side of the sample, and $\underline{\underline{I}}$ is the unit tensor. As for the initial conditions, the velocity is everywhere set to zero at $t = 0$.

Table 1
Characteristics of the meshes used in the simulations

	Elements	*Nodes*	*Unknowns*
Mesh 1	100	441	983
Mesh 2	196	841	1879
Mesh 3	256	1089	2435
Mesh 4	400	1681	3763
Mesh 5	576	2401	5379

3. Numerical method

The governing equations are solved in Lagrangian coordinates, which implies that the unknown position of the free surface is calculated automatically. The equations are discretized using the mixed-Galerkin finite element method with standard nine-node quadrilateral elements for the velocity and four-node ones for the pressure. The resulting non-linear system of equations is solved using a Newton–Raphson iteration procedure coupled to an iterative solver, with an error tolerance equal to 10^{-4}. Remeshing is achieved by using a Laplace-type discretization algorithm, i.e. the mesh is updated according to the new position of the free surface by solving $\nabla^2 y_i = 0$ and $\nabla^2 x_i = 0$ where the independent coordinates are those of a regular square (ξ, η) formed by the four corners of the domain. The mesh moves and its shape changes with the fluid velocity. When nodes of the free surface touch the solid boundary (in either side) the mesh is regenerated using a "rough" elliptic distortion, where interior nodes are placed at the average location of all their neighbours. Note that this is an iterative procedure until the mesh converges. Prior to the interior node generation, the boundary nodes are distributed so that the mesh is finer near the corners. The flow field variables are reassigned new values based on the old mesh.

4. Numerical results

In the numerical simulations, the finite amount of a Bingham plastic is compressed from rest (under either constant load or constant velocity) up to a time the flow becomes relatively very slow. Five meshes, the characteristics of which are tabulated in Table 1, have been employed, in order to study the convergence of the numerical results with mesh refinement. Fig. 2 shows typical mesh shapes obtained with Mesh 3 (16×16 elements) during an experiment under constant load with $Re = 1$, $Bn = 1$ and $M = 300$. It should be noted that the mesh appears to be more refined due to the fact that the graphics package we used divides each nine-node element into four quadrilaterals. Our numerical experiments have shown that Mesh 3 gives practically converged results. An example of the effect of mesh refinement is provided in Fig. 3, which shows the evolution of the sample height under constant load for Meshes 1 and 5, different Reynolds numbers (0.1, 1 and 10), $Bn = 0.5$ and $M = 300$. Our calculations showed that Meshes 3 and 5 (with respectively 256 and 576 elements) give essentially the same results. All subsequent numerical results have been obtained with Mesh 3.

The effect of the growth parameter M on the numerical results has also been studied. As already mentioned, M should be sufficiently high so that the regularized Papanastasiou model provides a good approximation of the ideal discontinuous Bingham model. On the other hand, very high values of M are undesirable since they lead to convergence difficulties [3,4,6]. Fig. 4 shows the effect of M on the evolution of the sample's height in a constant-load experiment for different Reynolds numbers and $Bn = 0.5$. For all the values of the Reynolds number, the numerical results for $M = 100$ and 800 are essentially the same.

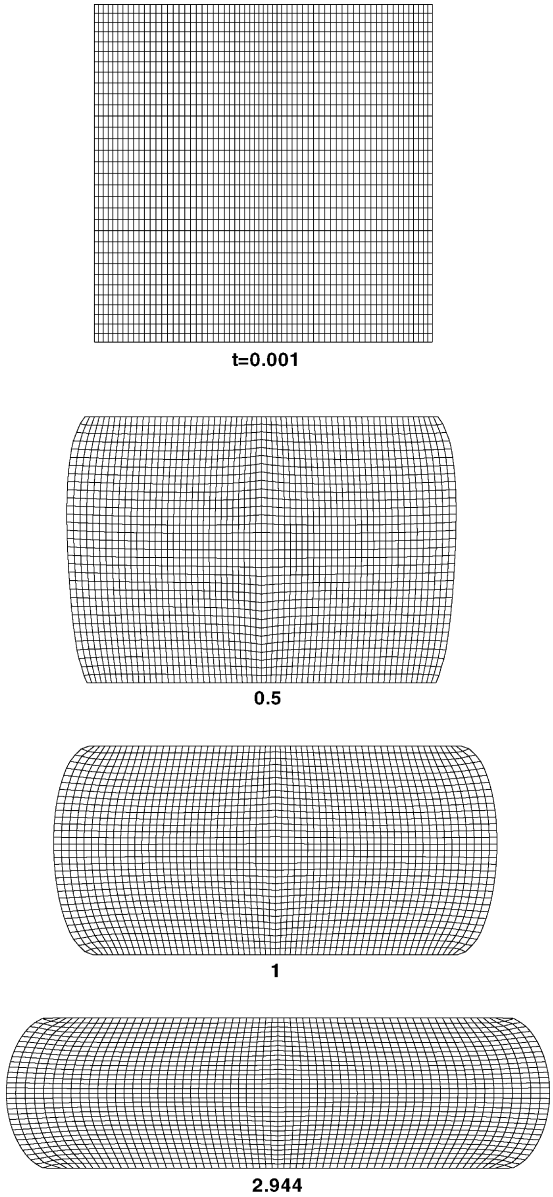

Fig. 2. Typical mesh shapes with 256 elements obtained in a constant-load experiment for $F = -10$, $Re = 1$, $Bn = 1$ and $M = 300$.

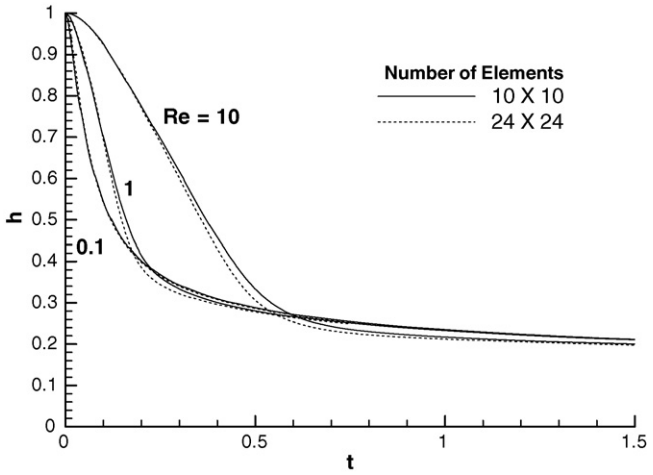

Fig. 3. Effect of mesh refinement on the evolution of the sample's height in a constant-load experiment for different Reynolds numbers, $F=-10$, $Bn=0.5$ and $M=300$.

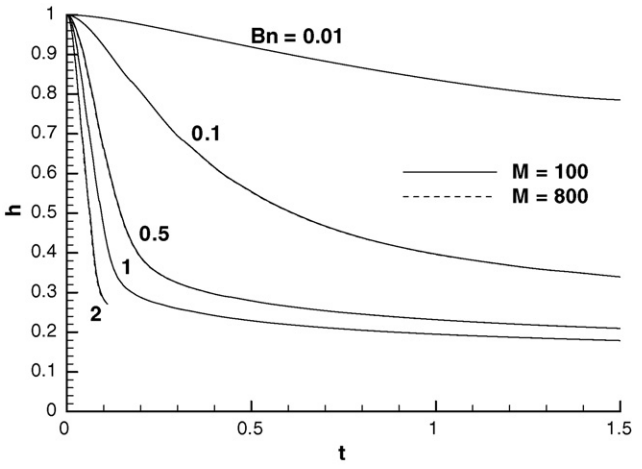

Fig. 5. Effect of M on the evolution of the sample's height in a constant-load experiment for different Bingham numbers, $F=-10$ and $Re=1$.

Fig. 5 shows the effect of M on the evolution of the sample's height for $Re=1$ and different Bingham numbers. Again, the results for $M=100$ and 800 are identical. This is also illustrated in Fig. 6, where we show snapshots of the sample at different times for $F=-10$, $Re=1$, $Bn=0.5$. The yielded and unyielded regions are also shown. The yield surfaces (i.e. the surfaces on which $\tau=1$) are determined using the technique proposed by Burgos et al. [7]. In agreement with Matsoukas and Mitsoulis [14], the unyielded areas observed at initial times are reduced in size as M is increased. In all subsequent results, we take $M=800$.

Let us now elaborate on the effects of the Reynolds and Bingham numbers in the case of compression under constant load. As shown in Fig. 3, the rate of compression becomes slower as the Reynolds number is increased, which may sound counterintuitive. However, due to our nondimensionalization keeping all the other numbers constant and increasing the Reynolds number is simply equivalent to increasing the density of the fluid. The overlapping of the curves corresponding to different Reynolds numbers is due to the fact that the effective stress field in the sample is eventually reduced below the material's yield stress.

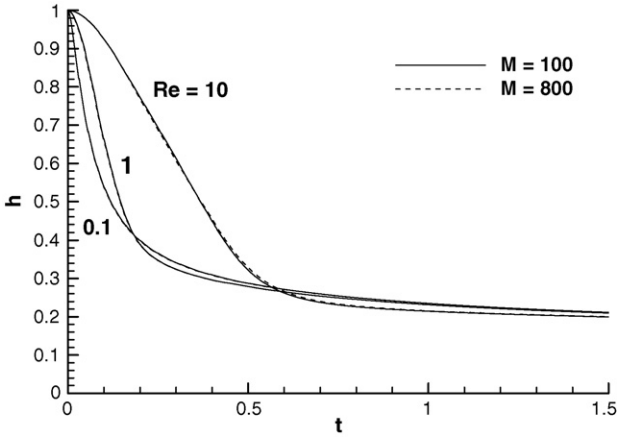

Fig. 4. Effect of M on the evolution of the sample's height in a constant-load experiment for different Reynolds numbers, $F=-10$ and $Bn=0.5$.

While the applied load is kept constant, the area of the sample's topside increases as the experiment proceeds and, therefore, the effective stress field decreases.

Fig. 7 shows snapshots of the sample and the corresponding yielded/unyielded regions taken at different times in a constant-load experiment ($F=-10$) for $Bn=0.5$ and $Re=0.1$, 1 and 10. As expected, the size of the unyielded spot at the bottom center decreases as the experiment proceeds. The compression of the sample begins soon after the whole material is yielded, with the exception of the unyielded spot located on the bottom around the symmetry axis of the sample. Even though this cannot be seen in the snapshots of Fig. 7, in the final stages of the experiment, unyielded regions appear on the top and the bottom around the symmetry axis; these grow fast and eventually meet causing the flow to stop (the material around the symmetry axis behaves as a rigid body). The upper part of the sample is initially more deformed than the bottom one, which is due to the fact that only the upper disk is moving. This asymmetry, which is more visible for high Re, moves towards the center of the sample as the experiment proceeds and the sample may look symmetric. In the final stages of the experiment, however, the lower part of the sample is more spread than the upper one.

In order to study the effect of the yield stress, with the nondimensionalization used, we have to increase, of course, the Bingham number and re-adjust accordingly the load so that the dimensionless number

$$F^* = F\,Bn = \frac{\bar{F}}{\mu U H} \tag{15}$$

remains constant. The deformation of the sample and the evolution of the yielded (grey) and unyielded (black) regions for $F^*=-10$, $Re=1$ and three Bingham numbers, 0.1, 1 and 2, are shown in Fig. 8. In general, the unyielded region initially appears around the axis of symmetry at the fixed bottom side of the sample and increases in size as the yield stress is increased reaching the periphery of the sample. This observation is in agreement with the creeping-flow results of Karapetsas and Tsamopoulos [16]. At higher Bingham numbers an unyielded spot is also

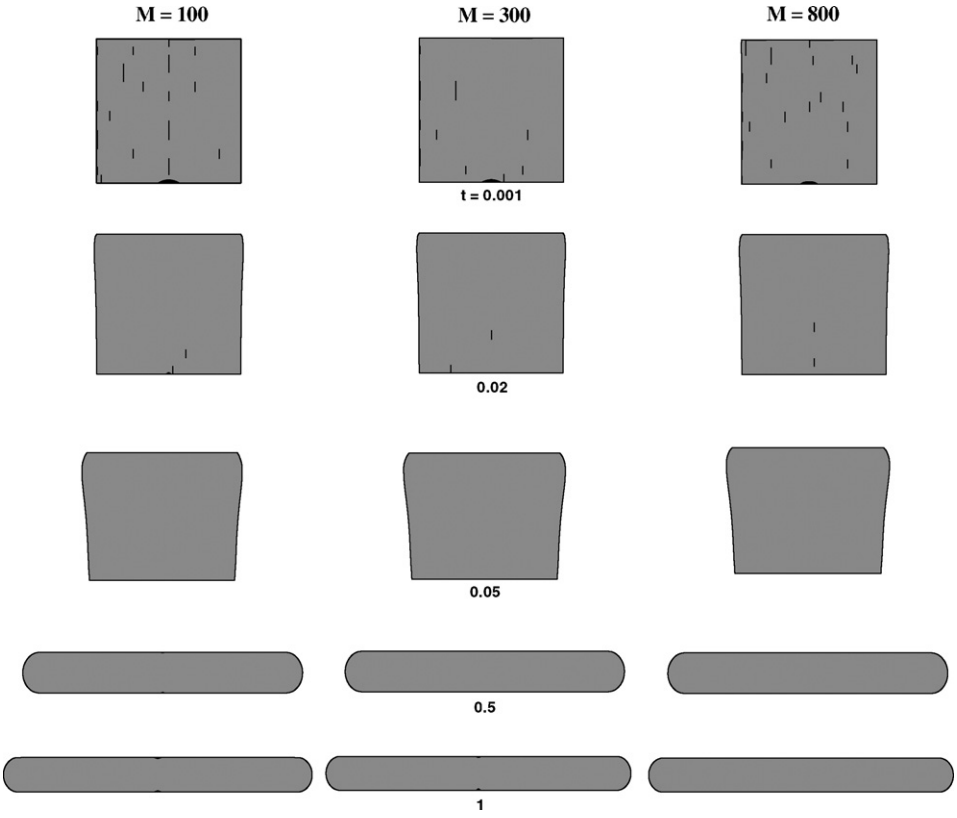

Fig. 6. Effect of M on the evolution of the yielded (grey) and unyielded (black) regions in a constant-load experiment with $Re = 1$, $Bn = 0.5$ and $F = -10$.

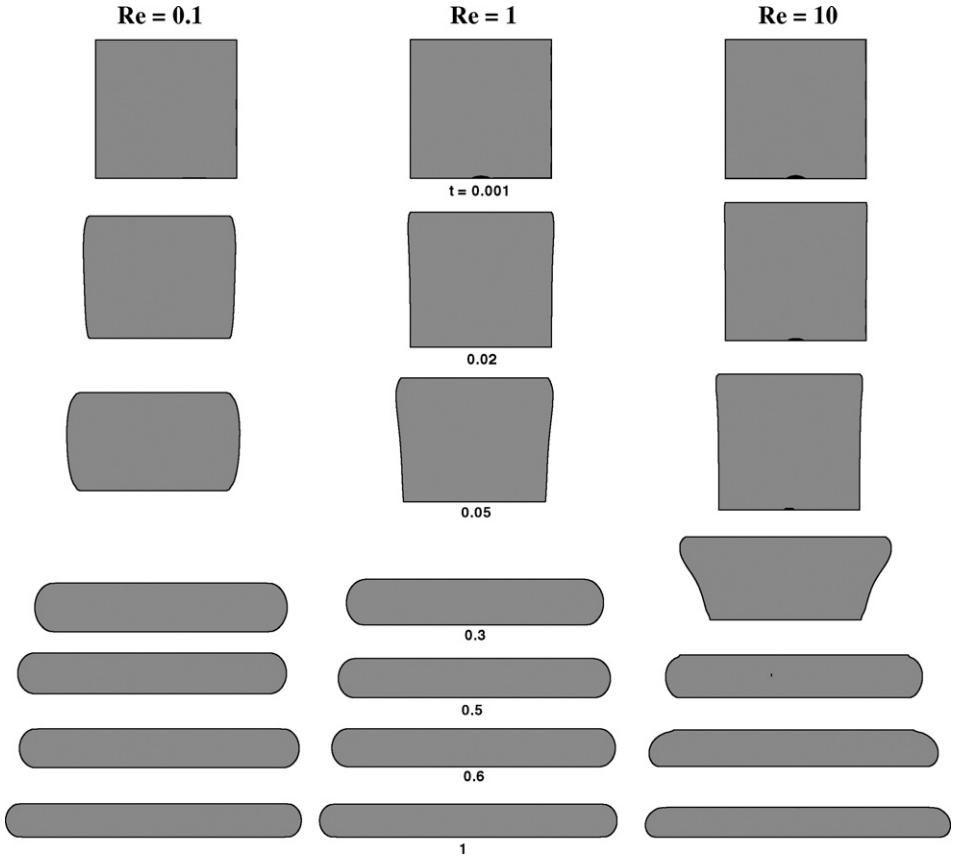

Fig. 7. Compression under constant load and evolution of the yielded (grey) and unyielded (black) areas for different Reynolds numbers, $F = -10$ and $Bn = 0.5$.

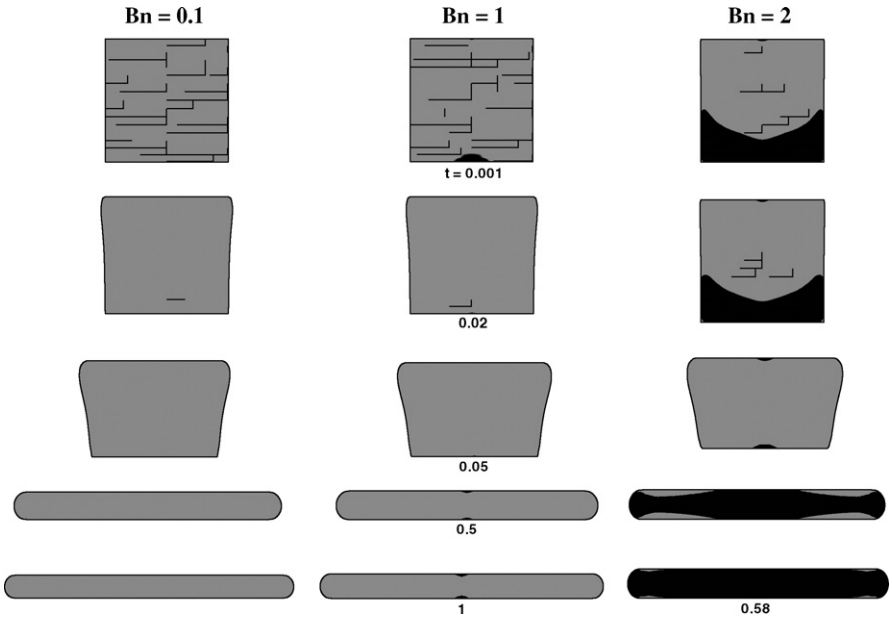

Fig. 8. Compression under constant load and evolution of the yielded (grey) and unyielded (black) areas for different Bingham numbers, $F^* = -10$ and $Re = 1$.

observed at the top side of the sample around the axis of symmetry. As clearly seen in the case of $Bn = 2$, unyielded regions grow again during the final stage of the experiment at the top and bottom sides of the sample around the axis of symmetry, which causes the flow to stop as they merge together. In fact, the flow stops early, at $t = 0.58$, as almost the entire material becomes unyielded and behaves as a rigid solid.

In Fig. 9, the rates of compression under constant load for $F^* = -10$, $Re = 1$ and three Bingham numbers, 1, 4 and 5, are shown. In agreement with the findings of Karapetsas and Tsamopoulos [16], the rate of compression decreases with the Bingham number and the experiment stops earlier due to the fact that the size of the unyielded region grows fast causing the flow to stop. Moreover, the final distance between the two disks increases with the Bingham number, which also agrees with the simulations of Karapetsas and Tsamopoulos [16].

Fig. 10 shows the effect of the applied load on the evolution of the sample's height for $Re = 10$ and $Bn = 0.5$. As expected, the rate of compression increases with the applied load. Interestingly, the compression with $F = -1$ is interrupted in the early stages of the experiment, as the effective stress field in the sample becomes lower than the yield stress.

It is clear that under constant velocity, compression starts instantaneously. In other words, almost all the material is yielded from the very beginning of the experiment, with the exception of a small unyielded spot that appears at the bottom side around the axis of symmetry. Fig. 11 shows snapshots of the sample obtained in constant-velocity experiments for a fixed Bingham number, $Bn = 0.5$, and $Re = 0.1$, 1 and 10. As expected, the shape of the compressed sample becomes more asymmetric at higher Reynolds numbers. The unyielded spot grows initially

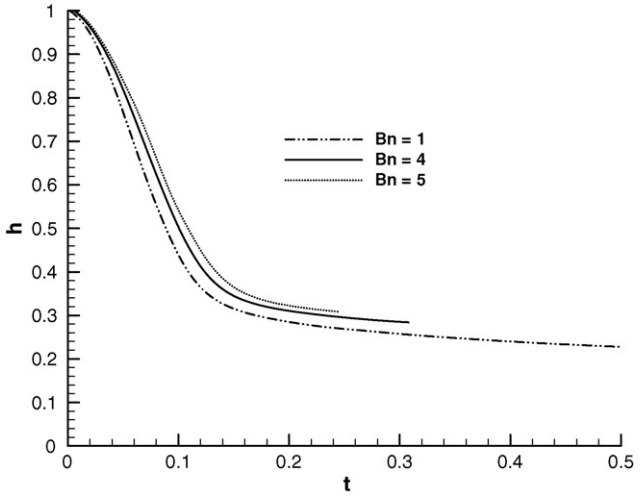

Fig. 9. Effect of the applied load on the evolution of the sample's height for $F^* = -10$ and $Re = 1$.

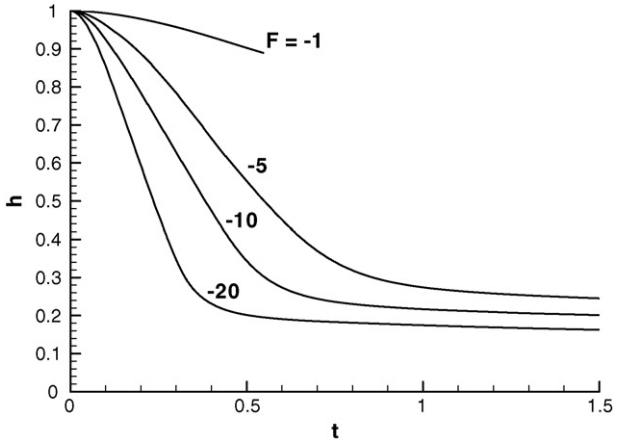

Fig. 10. Effect of the applied load on the evolution of the sample's height for $Re = 10$ and $Bn = 0.5$.

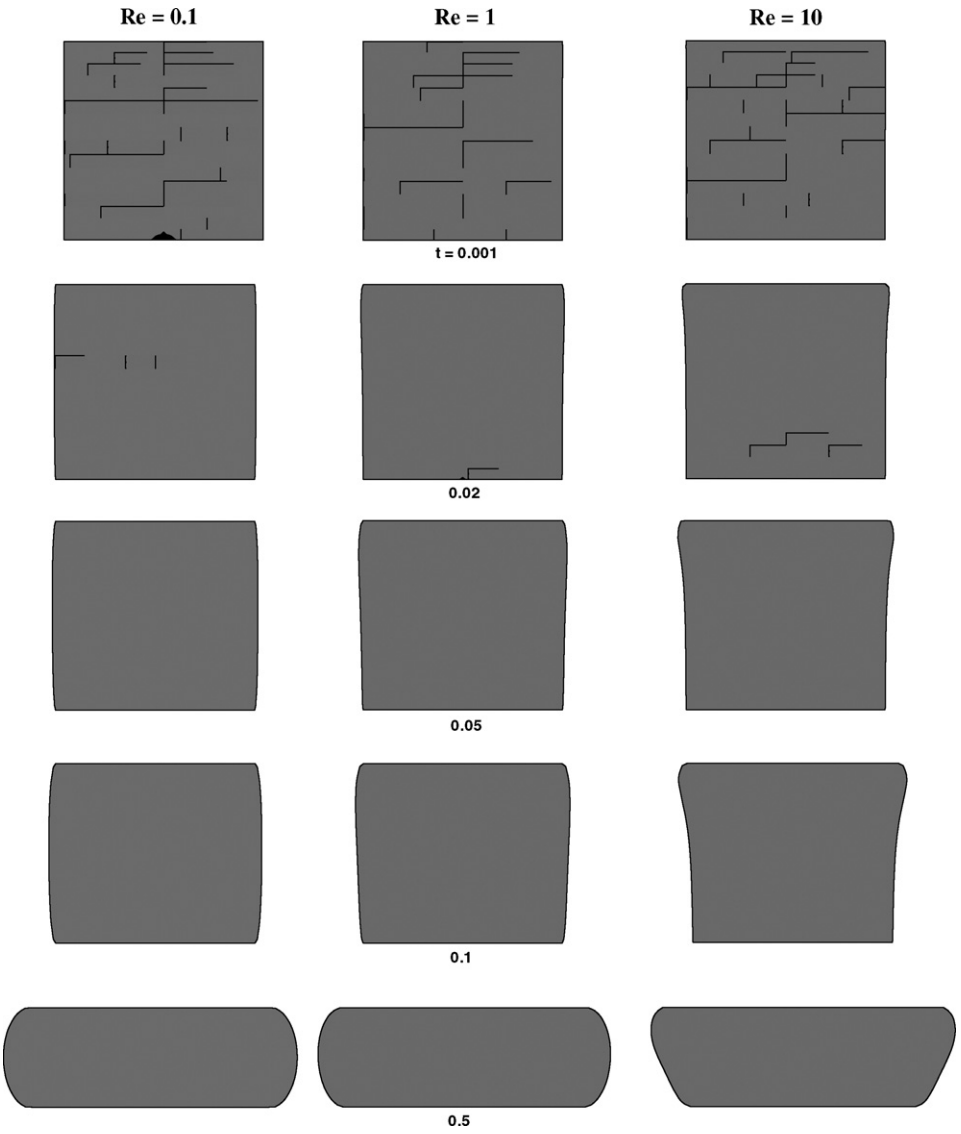

Fig. 11. Compression under constant velocity and evolution of the yielded (grey) and unyielded (black) areas for different Reynolds numbers and $Bn = 0.5$.

and then disappears. Its size is reduced as the Reynolds number is increased. Fig. 12 shows snapshots of the sample obtained for $Re = 10$ and various Bingham numbers (0.01, 0.1 and 1). In the case of $Bn = 1$, we observe again an unyielded spot around the axis of symmetry on the bottom side of the sample, which initially grows and then disappears.

Figs. 13 and 14 show respectively the effects of the Reynolds and the Bingham numbers on the resulting load along the topside of the sample during compression at constant velocity. Since there is no elastic component in the constitutive equation, the load required to maintain the constant velocity of the moving disk at $t = 0$ is very high (infinite in theory). However, the load decreases rapidly to reach a plateau in the initial stages of the experiment, and then increases sharply due to the rapid increase of the sample area. The numerical simulations fail to advance above a critical time, as the sample becomes very thin and the surface of the sample very large (the finite elements are of high aspect ratio). Note that smoothing has been used in order to eliminate artificial spikes in the pressure (and hence in the calculation of the load) due to the discrete advancing of the nodal points on the solid surface. This is clearly a disadvantage caused by the limitations of the remeshing technique used. With the exception of the initial decreasing regime, the observed behaviour of the load is consistent with the analysis of Sherwood and Durban [12] and the experiments of Adams et al. [13] with an elasto-viscoplastic material. Evidently, the sharp increase of the load in the final stages of the experiments is due to the increase of the area of the sample that is being compressed at constant velocity. Karapetsas and Tsamopoulos [16] also found that the applied force increases significantly with time, in their creeping-flow numerical simulations in which both plates were moving. They also noted that the load increases as the aspect ratio of the sample is increased, in agreement with previous works [10,15].

The necessary load to achieve compression at constant velocity increases with the Reynolds (Fig. 13) and the Bingham

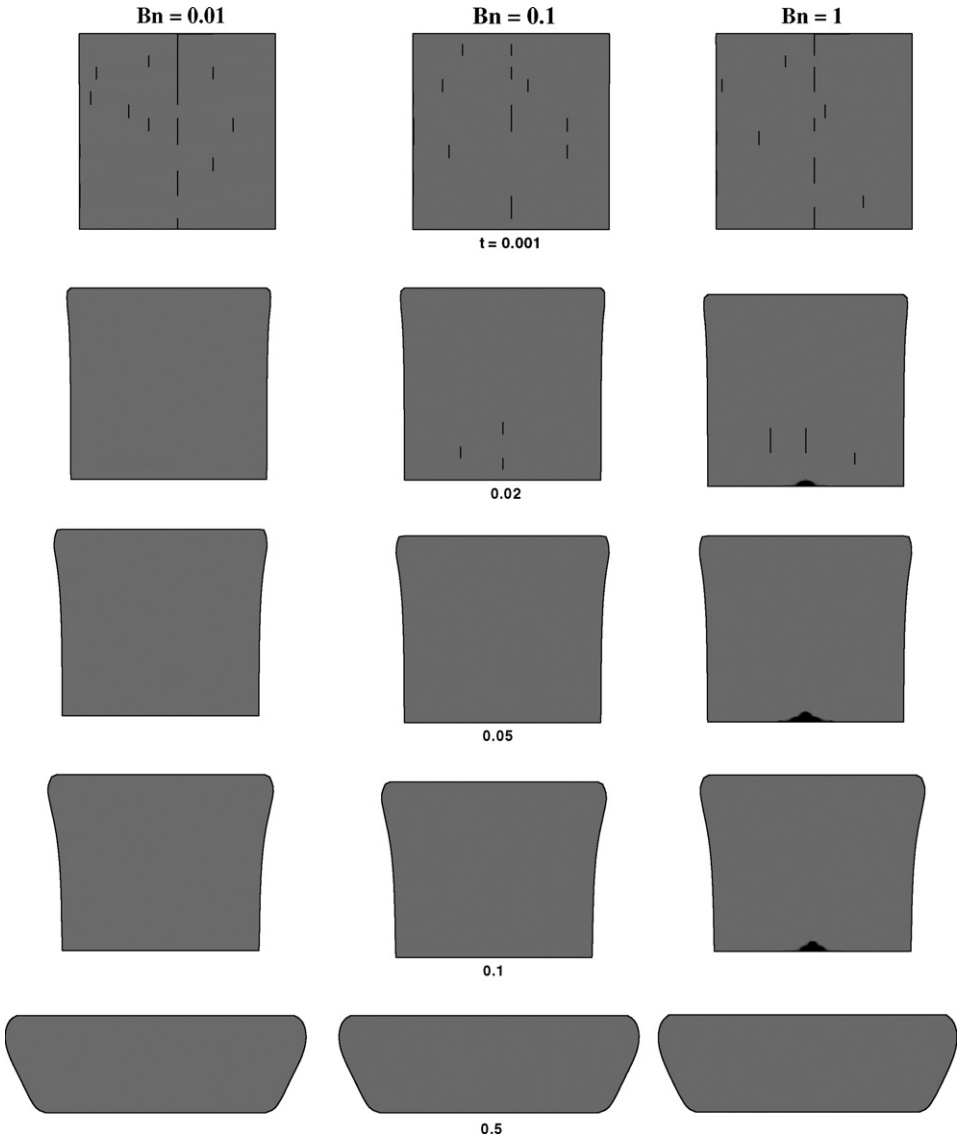

Fig. 12. Compression under constant velocity and evolution of the yielded (grey) and unyielded (black) areas for different Bingham numbers and $Re = 10$.

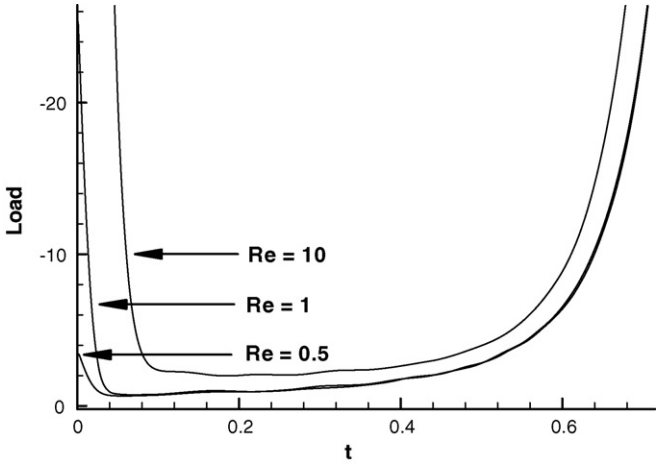

Fig. 13. Effect of the Reynolds number on the resulting load in a constant-velocity experiment for $Bn = 0.5$.

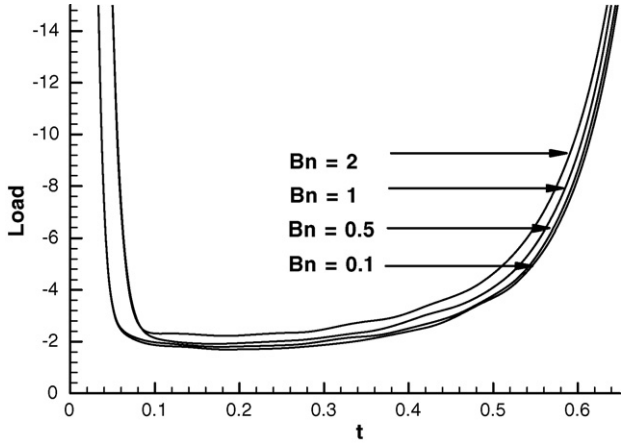

Fig. 14. Effect of the Bingham number on the resulting load in a constant-velocity experiment for $Re = 10$.

numbers (Fig. 14). In their creeping-flow simulations, Matsoukas and Mitsoulis [14] and Karapetsas and Tsamopoulos [16] also found that the load increases with the Bingham number, as expected.

5. Concluding remarks

We have simulated numerically the flow of a finite amount of a Bingham plastic, assuming that the top side of the sample is compressed either under constant velocity or constant load while its bottom side is fixed. The flow is modelled in Lagrangian coordinates employing the Papanastasiou regularization for the Bingham plastic and using a mixed-Galerkin finite element method.

The simulations under constant load showed that the unyielded regions are located around the axis of symmetry at the bottom side of the sample and their size increases with the Reynolds and the Bingham numbers. In the initial stages of compression, the unyielded area decreases in size and, in some cases, disappears completely. In the final stage of the compression, unyielded material is built again at the top and bottom sides of the sample causing the flow to stop. The rate of compression becomes slower as the Reynolds and Bingham numbers are increased.

When the sample is compressed with constant velocity, the material is yielded from the beginning of the experiment. The necessary applied load increases as the *Bn* and *Re* numbers are increased.

The numerical results for the flow and the shape of the test sample may be used together with experiments in order to determine the material constants. Given that the materials of interest exhibit thixotropic behavior, a more systematic study of the compression flow, including both experiments and simulations, is still required. Moreover, the evolution of the yielded and unyielded regions and the permanent damage of the material need to be further investigated.

References

[1] A.N. Alexandrou, Y. Pan, D. Apelian, G. Georgiou, Semisolid material characterization using computational rheology, in: Y. Tsutsui, M. Kiuchi, K. Ichikawa (Eds.), Proceedings of the Seventh International Conference on Semi-Solid Processing of Alloys and Composites, Tsukuba, Japan, 2002, p. 417.
[2] T.C. Papanastasiou, Flows of materials with yield, J. Rheol. 31 (1987) 385.
[3] K.R.J. Ellwood, G.C. Georgiou, T.C. Papanastasiou, J.O. Wilkes, Laminar jets of Bingham-plastic liquids, J. Rheol. 34 (1990) 787.
[4] A.N. Alexandrou, T.M. McGilvreay, G. Burgos, Steady Herschel–Bulkley fluid flow in three-dimensional expansions, J. Non-Newtonian Fluid Mech. 100 (2001) 77.
[5] G.R. Burgos, Rheology of semisolid metal suspensions, PhD Thesis, Worchester Polytechnic Institute, 1999.
[6] I.A. Frigaard, C. Nouar, On the usage of viscosity regularization methods for visco-plastic fluid flow computation, J. Non-Newtonian Fluid Mech. 127 (2005) 1.
[7] G.R. Burgos, A.N. Alexandrou, V. Entov, On the determination of the yield surfaces in Herschel–Bulkley fluids, J. Rheol. 43 (1999) 463.
[8] D.K. Gartling, N. Phan-Thien, A numerical simulation of a parallel-plate plastometer, J. Non-Newtonian Fluid Mech. 14 (1984) 347.
[9] E.J. O'Donovan, R.J. Tanner, Numerical study of the Bingham squeeze film problem, J. Non-Newtonian Fluid Mech. 15 (1984) 75.
[10] D.N. Smyrnaios, J.A. Tsamopoulos, Squeeze flow of Bingham plastics, J. Non-Newtonian Fluid Mech. 100 (2001) 165.
[11] N. Roussel, C. Lanos, Z. Toutou, Identification of Bingham fluid flow parameters using a complex squeeze test, J. Non-Newtonian Fluid Mech. 135 (2006) 1.
[12] J.D. Sherwood, D. Durban, Squeeze-flow of a Herschel–Bulkley fluid, J. Non-Newtonian Fluid Mech. 77 (1998) 115.
[13] M.J. Adams, I. Aydin, B.J. Briscoe, S.K. Sinha, A finite element analysis of the squeeze flow of an elastoplastic paste material, J. Non-Newtonian Fluid Mech. 71 (1997) 41.
[14] A. Matsoukas, E. Mitsoulis, Geometry effects in squeeze flow of Bingham plastics, J. Non-Newtonian Fluid Mech. 109 (2003) 231.
[15] E. Mitsoulis, A. Matsoukas, Free surface effects in squeeze flow of Bingham plastics, J. Non-Newtonian Fluid Mech. 129 (2005) 182.
[16] G. Karapetsas, J. Tsamopoulos, Transient squeeze flow of viscoplastic materials, J. Non-Newtonian Fluid Mech. 133 (2006) 35.
[17] K.J. Zwick, P.S Ayyaswamy, I.M. Cohen, Variational analysis of the squeezing flow of a yield stress fluid, J. Non-Newtonian Fluid Mech. 63 (1996) 179.